JOURNAL OF GEOPHYSICAL RESEARCH, VOL. 113, A09216, doi:10.1029/2007JA013013, 2008

Diurnal variation in plasmaspheric He^+ inferred from extreme ultraviolet images

David A. Galvan,[1] Mark B. Moldwin,[1] and Bill R. Sandel[2]

Received 29 December 2007; revised 30 May 2008; accepted 25 June 2008; published 11 September 2008.

[1] A diurnal variation in He^+ density is observed using successive snapshots of the plasmasphere taken by the extreme ultraviolet (EUV) imager on the IMAGE spacecraft. Analysis of average EUV photon counts from a specific patch of plasma, which may move at a rate other than corotation, centered at L = 2.5 and L = 3.5 over successive images during an IMAGE pass, allows us to follow a flux tube and track the brightness variation across ~6–10 h of local time. These EUV brightness observations are converted to He^+ column-integrated densities by taking into account solar EUV flux as measured by the SOHO spacecraft. Variations in He^+ column density with local time provide insight into the process of plasmaspheric refilling by ionospheric plasma outflow on diurnal time scales. An analysis of 128 orbits of IMAGE EUV data in 2001 reveals that EUV photon count, and hence column-integrated He^+ density, tends to increase soon after dawn, decrease or stagnate around noon, and strongly increase in late afternoon through dusk. These observations show no significant dependence on geomagnetic activity and support the idea that diurnal refilling of the plasmasphere is largely controlled by increased photoionization at dawn by exposure of the ionosphere to sunlight. Azimuthal profiles of individual EUV images provide additional evidence for the same trend observed in the tracking technique and show that He^+ column abundance values are typically 50–100% higher at dusk than dawn.

Citation: Galvan, D. A., M. B. Moldwin, and B. R. Sandel (2008), Diurnal variation in plasmaspheric He^+ inferred from extreme ultraviolet images, *J. Geophys. Res.*, *113*, A09216, doi:10.1029/2007JA013013.

1. Introduction

[2] The plasmasphere is a toroidal population of cold, dense plasma enveloping the Earth. Its inner boundary is at an altitude of several thousand kilometers, where ion composition changes from O^+-dominated in the topside ionosphere to H^+-dominated in the plasmasphere. The location of the outer boundary, the plasmapause, can vary between L-shell of ~2–7 depending on geomagnetic activity [*Moldwin et al.*, 2002]. During periods of enhanced geomagnetic activity, the plasmapause is recognizable as a sharp density gradient. In quiet times, the density gradient can be mild enough to be indistinguishable from an exponential or power-law decrease with distance from the Earth [*Carpenter and Anderson*, 1992; *Moldwin et al.*, 2003, and references therein].

[3] The source of plasmaspheric plasma is the Earth's ionosphere. Photoionization and heating of ionospheric particles by solar extreme ultraviolet (EUV) increases the temperature of some ions enough that they expand outward into space, leaving the gravitationally bound atmosphere. As charged particles, they gyrate around the geomagnetic field and flow outward into space. Since more ions will be energized after dawn, when the ionospheric end of a flux tube begins receiving solar EUV, one expects the density of plasma in a given flux tube to increase as it moves from dawn to dusk across the day side. Though the upward flux of certain species of ions from the ionosphere has been modeled [*Bailey et al.*, 1979; *Richards and Torr*, 1985; *Guiter et al.*, 1991], and diurnal variation in plasmaspheric mass density has been inferred via ground based field-line resonance studies [*Menk et al.*, 1999; *Moldwin and Berube*, 2004], actual diurnal variation in plasmaspheric density has not yet been globally monitored. *Park et al.* [1978] used whistler observations to sample the electron density of the plasmasphere, finding a detectable diurnal variation at L = 3 during June 1973, but not at higher L. They concluded the diurnal variation in outward flux from the ionosphere was not enough to affect the average density along plasmaspheric flux tubes outside of L = 3 on a diurnal time scale, and that day-to-day density variations due to storms and substorms dominated the behavior.

[4] With the advent of EUV imaging from the IMAGE spacecraft, global remote sensing of plasmaspheric He^+ concentration has become possible over a broad range of local times and L-shells. EUV images of the Earth's plasmasphere have aided in the qualitative understanding of low energy (~1 eV) charged particle behavior in the inner magnetosphere. Observations of plasmaspheric plumes

[1] Institute of Geophysics and Planetary Physics, Department of Earth and Space Sciences, University of California, Los Angeles, California, USA.
[2] Lunar and Planetary Laboratory, University of Arizona, Tucson, Arizona, USA.

0148-0227/08/2007JA013013$09.00

[*Sandel et al.*, 2001; *Foster et al.*, 2002; *Garcia et al.*, 2003], azimuthal variations in density [*Goldstein et al.*, 2004], and the location of the plasmapause [e.g., *Yizengaw et al.*, 2005] have been useful in corroborating results of in situ spacecraft and ground-based instruments. However, quantitative photometry using EUV brightness within the plasmasphere has seldom been pursued [*Clilverd et al.*, 2003; *Gallagher et al.*, 2005; *Grew et al.*, 2007; *Sandel and Denton*, 2007]. In studies where it has, case study refilling rates for post-storm recovery were estimated, or average densities over seasonal or annual time scales were noted, but typical quiet-time diurnal variation observed over numerous events was not addressed. This study uses EUV images to infer the diurnal density variation of He^+ column abundance, via EUV brightness, in the dayside plasmasphere at L-shells of 2.5 and 3.5. The effects of departures from perfect corotation are taken into account.

2. Methodology

2.1. Data Selection

[5] The EUV instrument on board the IMAGE spacecraft consists of three cameras sensitive to extreme ultraviolet radiation at a wavelength of 30.4 nm. Solar EUV is resonantly scattered by He^+ ions in the Earth's plasmasphere. Because the plasmasphere is optically thin, the column-integrated brightness of scattered EUV photons as viewed from the spacecraft is directly proportional to the density of He^+ ions integrated along the EUV instrument's line of sight [*Sandel et al.*, 2000, 2001]. Hence brightness changes in an EUV image generally correspond to density variations in the plasmasphere.

[6] The general methodology of this study is to track a patch of plasma, a flux tube, as it moves across the dayside of the plasmasphere. In order to monitor the brightness, and hence density, of a particular flux tube in the plasmasphere as it rotates with the Earth, a consecutive series of images looking down on the plasmasphere from a perspective at high magnetic latitude is needed. The longer the EUV imager observes the plasmasphere from high magnetic latitude, the longer a patch of plasma can be accurately tracked. Also, since the column-integrated density of He^+ determines the intensity in an EUV pixel, the regions of density dominating these brightness values are concentrated relatively close to the geomagnetic equator when IMAGE is observing from high magnetic latitude and a large distance from the Earth. To optimize the EUV data quality, our survey of EUV images is constrained to periods when the IMAGE spacecraft has a polar apogee.

[7] The IMAGE spacecraft is in an elliptical polar orbit with its orbital normal fixed in inertial space. It has an apogee of $\sim$8.2 R_E (45,922 km altitude), and a perigee of $\sim$1.2 R_E ($\sim$1,275 km altitude). These orbital parameters result in a period of 14.2 h, however the EUV instrument is not operated for the entire orbit. The field-of-view (FOV) of the EUV instrument was designed to encompass the entire plasmasphere when viewing from apogee, where the spacecraft naturally spends most of its time. When IMAGE is at L-shell values less than $\sim$13, EUV is subject to high levels of radiation noise, hence the high voltage to the detectors is adjusted on the basis of the L-shell position of the spacecraft: high voltage to operating levels as the spacecraft moves to L-shells higher than L = 13 on the outbound leg of the orbit, and high voltage to reduced levels when it passes L = 14 on the inbound leg. With the 14.2-h orbit of IMAGE and the 24-h rotation period of the Earth, the spacecraft finds itself in a slightly different orientation of the geomagnetic field each orbit, and hence the duration of EUV imaging data taken varies from orbit to orbit. The duration of EUV imaging time ranges from less than 1 h in the period soon after IMAGE's launch in 2000, up to $\sim$9–10 h when IMAGE has a polar apogee.

[8] As a result of these limitations in EUV data availability, the full 12-h coverage required to track a flux tube from dawn to dusk is impossible for the IMAGE satellite in a single orbit. It is, however, possible to get periods of up to $\sim$10 h during which IMAGE dwells over the pole in a time period surrounding apogee. Due to the 50 degree/year precession rate of the orbit's line of apsides, IMAGE had a north polar apogee in the middle of 2001. This study includes a survey of EUV images throughout the year 2001, when the high latitude of IMAGE's orbital apogee made conditions optimal for diurnal flux tube tracking.

[9] Even when the EUV instrument is operating for a long period of time, the images taken during a given pass may not be usable for photometry. Solar energetic particle events, strong geomagnetic storm activity, and the Sun entering one or more of the three EUV sensors' field of view can all affect the EUV image quality. Hence a visual survey of the EUV data was done.

[10] Appendix A shows a list of the data intervals used in this study. To obtain this list of selected events, the 2001 EUV online catalog was visually surveyed for single IMAGE satellite passes containing EUV images without major data defects, such as sunlight contamination or oversaturated images, and during which all three EUV sensors were operating for the entire pass. The resulting list was then used to re-survey those events, selecting passes where 6 h or more of EUV images were available. The minimum duration of 6 h was chosen somewhat arbitrarily, keeping in mind that the longer the duration of good data in a given pass, the longer a flux tube can be tracked, but also that it is desirable to analyze enough events to be statistically significant. In addition, since tracking a flux tube requires determining the rotation rate of the plasmasphere, images in which the plasmasphere has some sort of localized density enhancement or depletion, such as a ''notch'' of low-density plasma, which can be tracked as it drifts around the Earth, are more useful than those in which the plasmasphere appears azimuthally homogeneous.

[11] The resulting list in Appendix A is centered around June of 2001, as this was the time period when IMAGE's orbital apogee was roughly over the north magnetic pole, allowing EUV to deliver long duration observations between its L-dependent high-voltage up and high-voltage down times. When the final list of intervals in Appendix A was produced, we used one image per hour within those intervals for flux tube brightness monitoring.

2.2. Data Processing

[12] Once an IMAGE pass (event) has been selected and added to the database, the EUV images must be processed further before azimuthal brightness profiles can be extracted. First, a background subtraction routine is applied

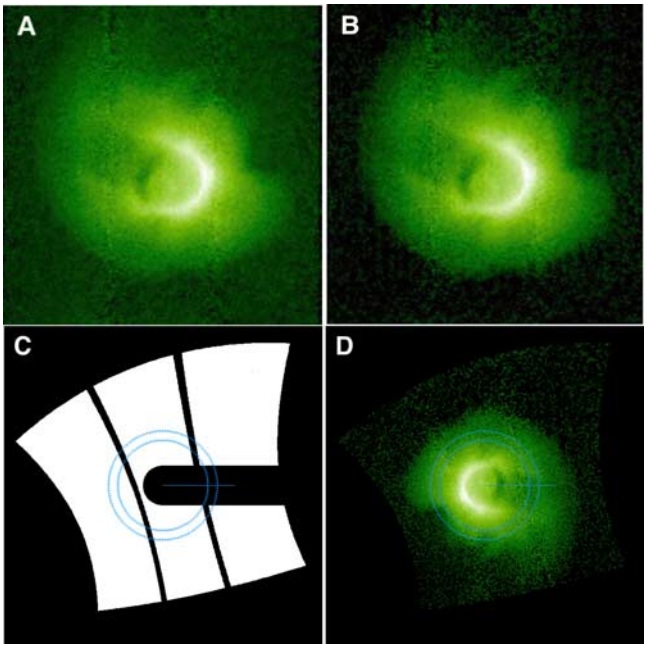

Figure 1. Illustration of EUV data processing for an image taken at 2001/173/02:25 UT. (A) Original EUV FITS file available from the EUV database. (B) The same image after background subtraction. (C) The shadow mask, where black regions represent parts of the EUV image that will be ignored. (D) Final image, mapped to the geomagnetic equatorial plane, showing the L = 2.25 to 2.75 region from which azimuthal brightness profiles will be extracted.

to each image. Figures 1A and 1B show examples of an original EUV image and its background-subtracted version, respectively. The intent of background subtraction in this case is to reduce the uncertainty stemming from the possibility that one EUV image might be much brighter than the next because of changes in the scattered sunlight contamination. In such a case, the difference in brightness between one image and another would not be entirely due to density variations in the plasmasphere.

[13] The background-subtracted images are mapped to the geomagnetic equator using dipole geomagnetic field geometry, where the brightness value of each pixel is re-positioned. Each pixel in a given image represents a specific line-of-sight of the EUV instrument through the plasmasphere. Using the known position of IMAGE relative to the Earth, the direction of the line of sight of each pixel, and a simple dipole magnetic field model, the mapping function solves for the corresponding lowest L-shell field line touching the line of sight. The original pixel brightness value for that line of sight is then plotted at the L-shell (radial) and magnetic local time (azimuthal) coordinates of that geomagnetic field line. This method of mapping magnetospheric images was described by *Roelof and Skinner* [2000], and applied to EUV images by *Sandel et al.* [2003]. The result is a magnetic-polar projection of the original EUV image [e.g., *Goldstein et al.*, 2003]. In addition, meta-data in each EUV data file allows the mapping routine to create a shadow-mask image defining the regions of the mapped image which are unreliable for photometry. These regions include the Earth's shadow, where brightness values are lower because of reduced illumination by solar EUV, and the two areas of seam overlap between the three EUV sensors. The seams in a given EUV image are of lower photometric accuracy owing to vignetting at the edges of the fields, and to overlap at the edges of the three EUV sensors. In later data processing, the shadow-mask image produced during the mapping process is used to allow us to ignore the data in the specified seam and shadow regions when taking azimuthal brightness profiles.

[14] Figure 1C shows an example of a shadow-mask image. The warped appearance of the outer edge of the image is a consequence of projecting the original EUV image to the geomagnetic equatorial plane using dipole field geometry. The Earth is at the center, with the thick, horizontal black bar extending from the center to the right representing the Earth's shadow. The two long, narrow bars stretching from the top to the bottom are the seams between the three EUV sensor fields of view. Pixels in the actual mapped EUV image that fall in the seams and shadow are not used for photometry in this study.

2.3. Data Analysis

[15] After the background-subtracted image is projected to the geomagnetic equator, average pixel brightness values are taken from the image in an annulus around the Earth with inner radius at L = 2.25 and outer radius at L = 2.75 (the blue circles in Figures 1C and 1D). The range in L-shell was chosen to be in the middle region of a quiet-time plasmasphere, allowing us to monitor the density of a somewhat uniform volume of plasma. Even in cases of moderate geomagnetic activity, all images used in this study show a plasmapause at L > 2.75, though density features like notches often intrude into the annulus, as will be discussed later. The inner boundary of the annulus was chosen to avoid taking brightness data from the region within L $\sim$ 2, where the EUV photons observed may be produced largely by airglow, and densities may be high enough that the particle population is no longer optically thin, such that a radiative transfer model would be required to infer column-integrated-densities.

[16] The annulus in each image is divided into 128 azimuthal bins, each 11.25 min wide in local time (LT). Figure 1D shows the background-subtracted, mapped EUV image with the 128 bin annulus in place. The standard deviation of the mean for the brightness value of pixels in a given bin is taken as a measure of the uncertainty of the mean brightness for that bin. An example of the brightness profiles generated by extracting the average brightness of the pixels in each bin is shown for multiple images in the same IMAGE pass in Figure 2. Note the distinct valley in brightness that starts between MLT 13 and 14 in the earliest profile, and makes its way to between MLT 21 and 22 in the latest profile. This is the signature of a "notch" of low-density plasma observed in Figures 1A, 1B, and 1D. Features like this are used to track the corotation rate of the plasmasphere, which is then used to monitor the brightness of a flux tube as it moves around the Earth.

2.4. Determining the Corotation Factor

[17] In order to be confident that we are tracking the same flux tube in our EUV images, the rotation rate of the

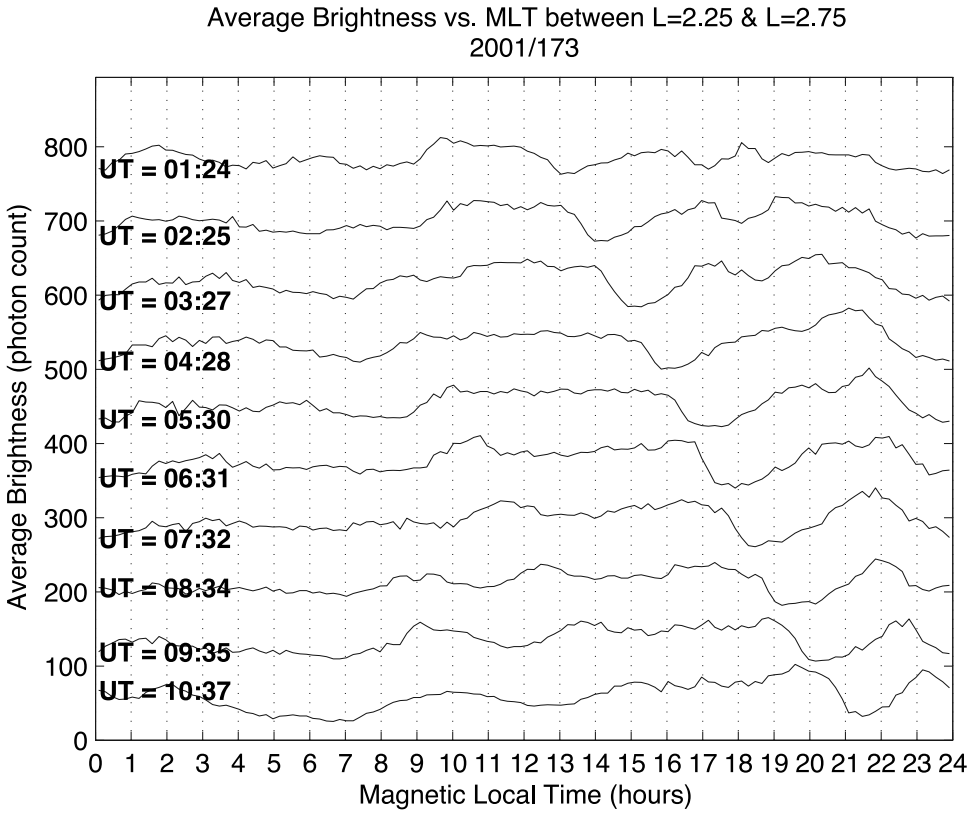

Figure 2. Average brightness vs. local time for an annulus including pixels between L = 2.25 and L = 2.75 for 10 consecutive hourly EUV images during a single orbital pass of the IMAGE spacecraft. The vertical axis is in units of photon counts but is only applicable to the bottom brightness profile. The other profiles are stacked for ease of comparison, earliest at the top (UT 01:24).

plasmasphere must be determined. *Sandel et al.* [2003] showed that density features in the plasmasphere have been observed to lag the corotation speed, moving as slow as 85% of corotation. *Gallagher et al.* [2005] later observed extreme cases of notches moving as slow as 44% of corotation. *Burch et al.* [2004] hypothesized that the cause of subcorotation is the Joule heating of the high latitude ionosphere by auroral precipitation, the initiation of equatorward winds, and the subsequent slowing of ionospheric plasma relative to the Earth's rotation due to conservation of angular momentum, a.k.a. the Coriolis effect. Superrotation of the topside ionosphere, from which plasmaspheric plasma originates, has also been observed at mid-latitudes [*Rishbeth*, 1972]. Detailed study of the cause of the variable rotation rate of the plasmasphere is beyond the scope of this paper, and will be re-visited in a future study. Here we simply measure the rotation rate to enable our monitoring of plasmaspheric flux tube density.

[18] If perfect corotation is assumed, plasma E × B drifting on closed flow paths should move 1 h eastward in local time (LT) over 1 h of Universal Time (UT). However, with a significant likelihood of subcorotation, determining the rotation rate of the plasmasphere is important for accurate flux tube tracking. The rotation rate is tracked using mean-removed cross-correlation of brightness profiles from several of the images in a given event. The determined rate is then assumed to be constant for the duration of that event, and to apply to all azimuths. In this study, the rotation rate is defined by a "corotation factor" = $(\Delta LT)/(\Delta UT)$; that is, the change in the local-time location of a plasmaspheric feature divided by the real time elapsed between the two EUV snapshots.

[19] Care must be taken when determining the corotation factor, as incorrect values will lead to monitoring the brightness of different regions of plasma in the EUV images, when a single flux tube is desired. In determining the corotation factor, part of the uncertainty depends on the resolution of the images themselves, and the amount of real time between EUV exposures. The uncertainty of our corotation factor is based on the uncertainty in the local time lag value (ΔLT) between brightness profiles that results in the maximum correlation coefficient. Given that each brightness value in an image profile is separated from the next one by 11.25 min of local time (24 h/128 bins = 11.25 min), ΔLT has an uncertainty of ±11.25 min. Therefore a given corotation factor has an uncertainty of ± (11.25 min)/(ΔUT). The uncertainty in our corotation factor will be smaller for larger time differences between images. For images separated only by 1 h, a corotation factor would have an uncertainty of ±0.19, meaning it is uncertain whether the plasmasphere is subcorotating by ∼19% or super-rotating by the same amount. Therefore deriving the corotation factor from images separated by only 1 h is unacceptable if meaningful accuracy is desired.

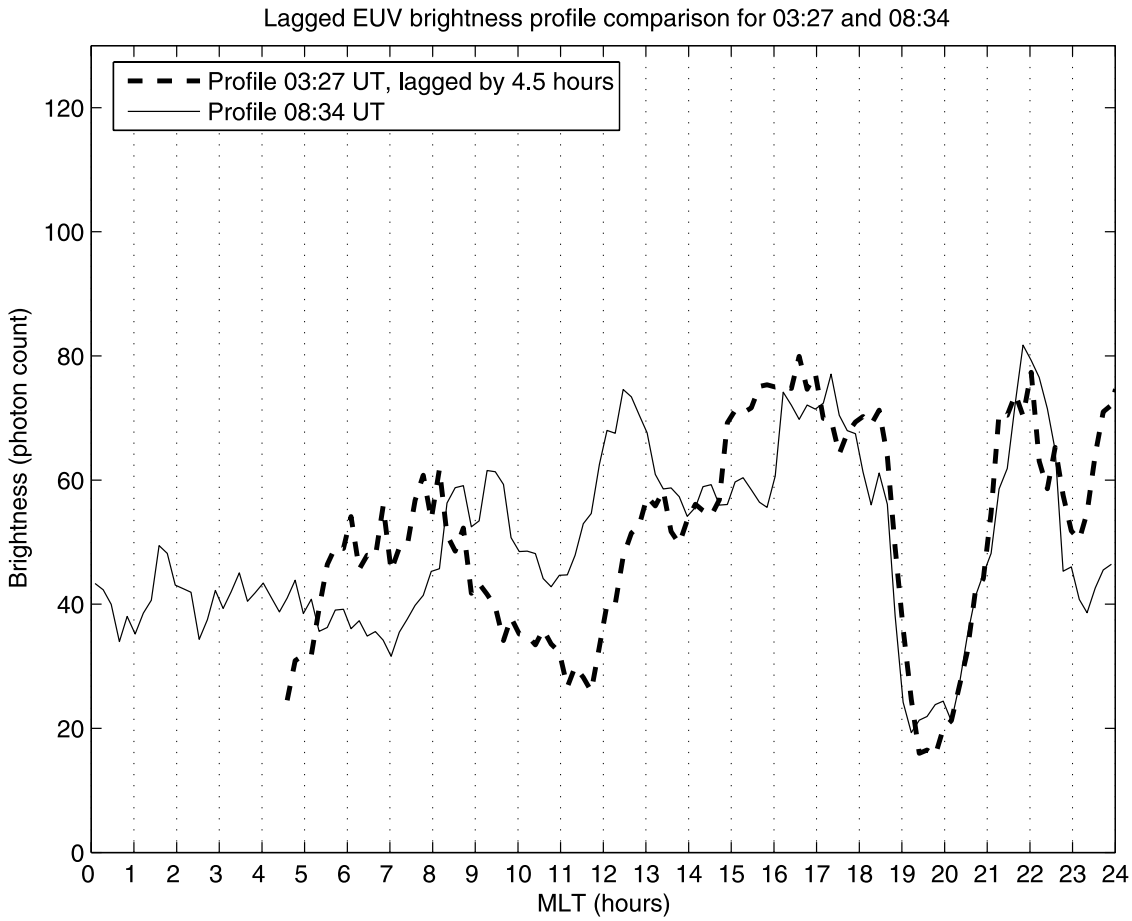

Figure 3. Two representative brightness profiles for day 173. The 03:27 profile has been lagged by 4.5 h, when the mean removed cross-correlation between the profiles is at a maximum value of 0.5 and the resulting corotation factor is 0.88.

[20] Determining the corotation factor by comparing the MLT location of features in images 24 h apart is not reliable for this study, because it would require we assume that the corotation rate did not change over more than twice our time range of interest. To be comfortable in our assumption of a constant corotation factor during a given event, we determine the corotation factor using only data from within that 6–10 h time period. The highest accuracy we can expect from a single pair of images within our time range is ±11.25 min/10 h = 0.019 ≈ ±2% corotation. However, as there would likely be, at most, one image pair in our set separated by 10 h, we make the more practical attempt to have our corotation factor be accurate to at least ±5% for each measurement. We accomplish this by taking every pair of hourly images within a given event separated by at least (0.19 h/0.05 =) 3.75 h and producing a corotation factor with its own unique uncertainty value. Every brightness profile in an event is cross-correlated with every other brightness profile as long as they are separated by more than 3.75 h. The lag between the two brightness profiles that yields the maximum correlation coefficient is taken to be the ΔLT for that pair of profiles. Since each brightness profile is associated with a specific EUV image, which was taken at a specific UT, the corotation factor can now be calculated. For example, when we perform a mean-removed cross-correlation between the brightness profiles for EUV images taken at 03:27 and 08:34, we find that the highest positive correlation coefficient is about 0.5, and occurs when 03:27 is shifted forward by 4.5 h. Therefore the earlier profile most resembles the later profile when it is shifted 4.5 h forward in time. This lag represents the ΔLT between the two profiles, while the ΔUT is simply 08:34–03:27 = 5 h, 7 min. The corotation factor is thus calculated as 0.879 ± 0.037 for this pair.

[21] Figure 3 shows a visual representation of the cross-correlation of two brightness profiles. The solid profile is from the image at 08:34 UT, while the dashed profile is from the 03:27 UT image. The two profiles were cross-correlated, and the earlier profile is displayed time-shifted by the lag value at which the maximum correlation coefficient occurs. Note that the maximum correlation coefficient occurs at a lag value of 4.5 h, and that this corresponds to the alignment of the low-density "notch" feature in the 03:27 profile with the same feature in the 08:34 profile. Hence dominant azimuthal density features in the plasmasphere drive the high correlation coefficient, and are useful for measuring the rotation rate of the plasmasphere.

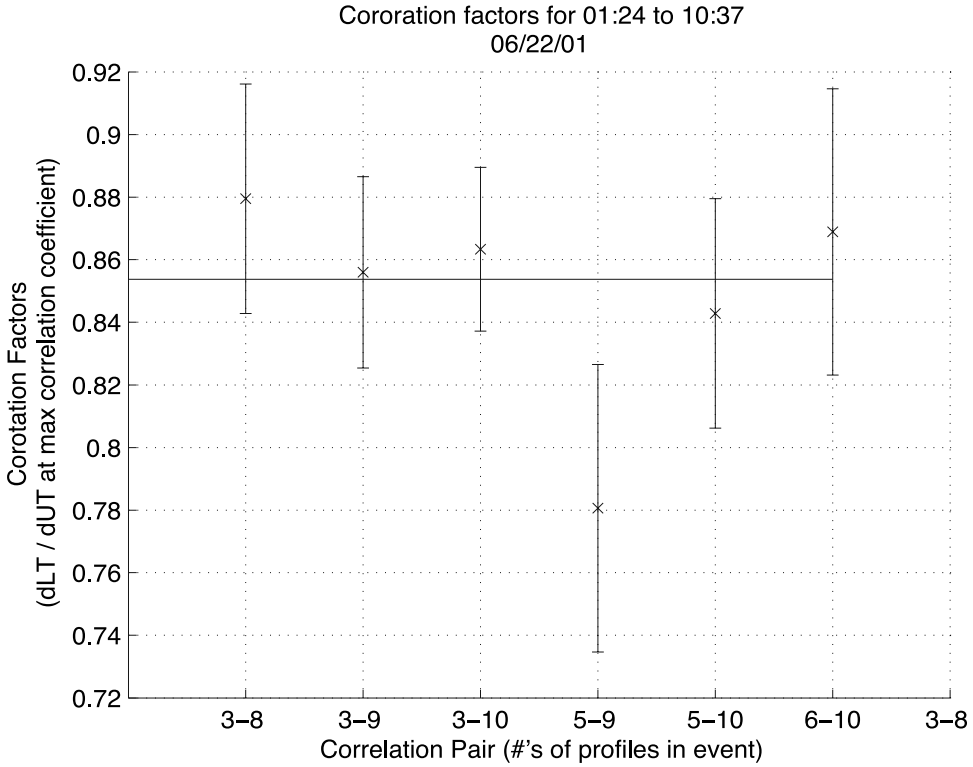

Figure 4. Corotation factors generated for the event day 173 01:24–10:37. The vertical axis represents the corotation factor value, and the horizontal axis represents the cross-correlation that has been performed. For instance, "3–8" means the 3rd brightness profile cross-correlated with the 8th brightness profile.

[22] Another source of uncertainty in our measurements of the corotation factor is the evolution of distinctive brightness features in the plasmasphere. In an ideal case, an azimuthal feature such as a notch in a specific region of magnetic longitude exists in all the images for an orbital pass. The entire plasmasphere is assumed to be rotating at the same rate as this plasmaspheric notch, and the cross-correlation technique is used to track how fast that feature, and therefore the plasmasphere, is rotating. Since the brightness levels and shape of the plasmasphere as viewed by the EUV instrument changes over a single orbital pass, any traceable feature may change morphology after several hours, thus making cross-correlation of brightness profiles less reliable. In order to further constrain which profile pair corotation factors will be averaged to determine the final corotation factor assigned to that event, we require a minimum correlation coefficient. If the morphology of the azimuthal structure of the plasmasphere has changed significantly in the time elapsed between the two profiles being cross-correlated, it will likely result in a low correlation coefficient. Hence in addition to the maximum uncertainty of ±5% of corotation, we impose a somewhat arbitrary minimum correlation coefficient of 0.5.

[23] Figure 4 shows the corotation factors that meet both the maximum uncertainty and minimum correlation coefficient constraints for the event 2001/173/01:24–10:37. The labels on the x-axis identify the particular brightness profiles being cross-correlated. The profile from the earliest image (in this case, 2001/173/01:24, the uppermost trace in Figure 2) is given the number 1, and subsequent profiles are numbered accordingly, so that a label of "1–5" means that corotation factor was derived by cross-correlation of the first and fifth brightness profiles for that event. The solid line represents the mean of these individually determined corotation factors, weighted by the individual uncertainty of each factor, and is used as the final corotation factor for that event. There are only a few corotation factors for which the uncertainty is less than ±0.05, and for which the correlation coefficient was greater than 0.5. The final corotation factor used in tracking the flux tubes for this event is 0.854 ± 0.014, indicating the plasmasphere was subcorotating by about 15%. Note that the uncertainty of 0.014 is the standard deviation of the weighted mean.

2.5. Following the Flux Tube

[24] Once the rotation rate of the plasmasphere is known, the brightness of an EUV line of sight, aligned with part of a plasmaspheric flux tube, can be monitored by taking the brightness value at a given MLT from the first image, then the brightness value at the MLT of the flux tube propagated by the observed corotation rate in the second image, and so on. To propagate to the MLT of the flux tube in a subsequent image, we simply take the difference in UT between the two snapshots, multiply it by the corotation factor, and add the product to the original MLT_0 of the flux tube in the first image. This yields the MLT in the subsequent image where we take the next brightness sample in our flux tube's

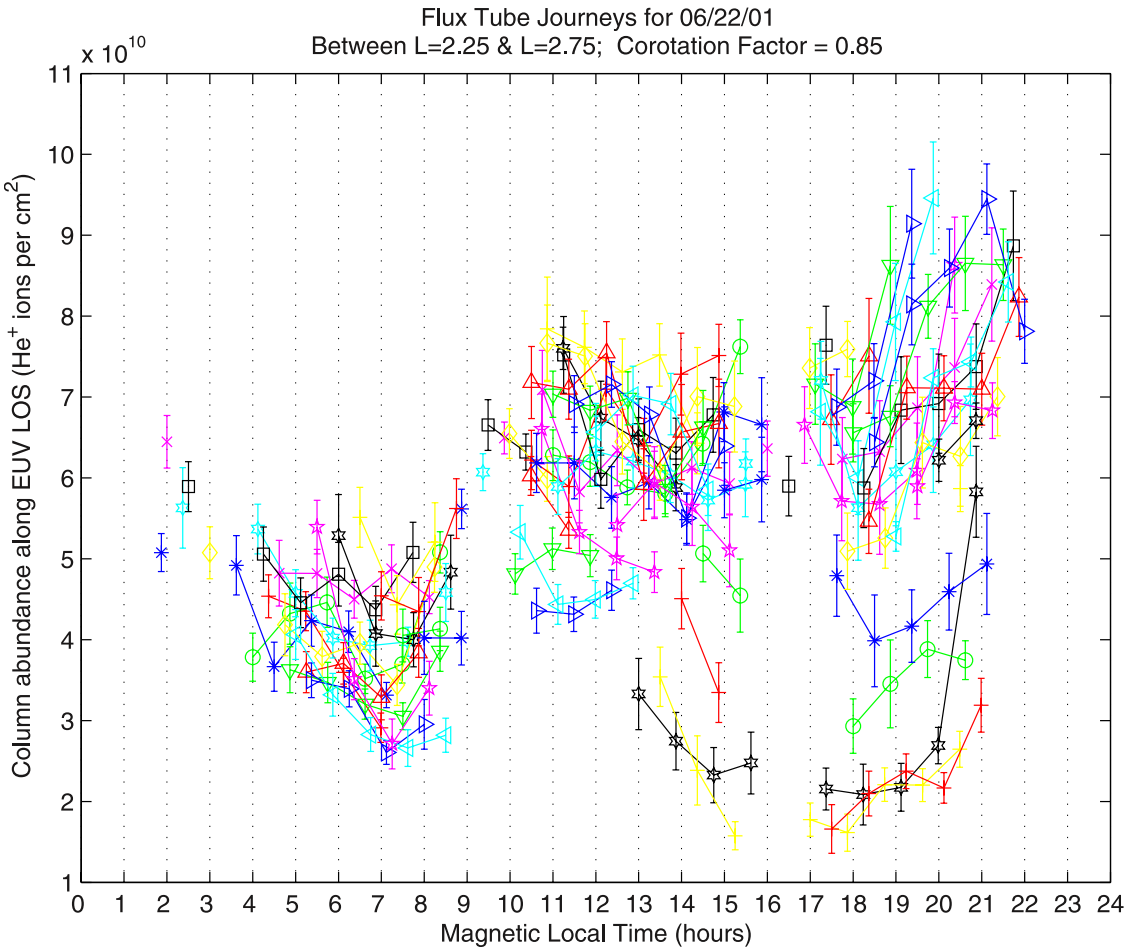

Figure 5. Flux tube journeys for the event 2001/173/01:24–10:37. Each connected set of points represents the line-of-sight He^+ column abundance through a flux tube as it moves around the Earth at ~85% corotation speed. Error bars are the standard deviation of the mean column abundance.

journey. In this way, brightness profiles of flux tube journeys are generated, each of which is composed of brightness values obtained from all the successive images in that event. It is worth noting that, when tracking the flux tubes, we assume that they do not vary in radial distance during their rotation around the Earth. This is equivalent to assuming a dipole geomagnetic field geometry, which we consider to be reasonable for the L-shells of interest: L = 2.5 and L = 3.5 [e.g., *Berube et al.*, 2006].

[25] We also convert from units of photon count to units of He^+ column abundance along the EUV line of sight. Since the plasmasphere is optically thin, the photon count in a EUV pixel whose line of sight goes through the plasmasphere is directly proportional to the column-integrated density of He^+. Hence we use the following conversion:

$$N = 2.76 \times 10^{19}\,(a/F)$$

where N is the column abundance of He^+ in units of particles cm^{-2}, a is the number of photon counts in a single pixel of an EUV image (10 min exposure), and F is the solar flux of 30.4 nm wavelength light at 1 AU, in units of photons s^{-1} cm^{-2}. The constant in the conversion equation is derived from a He^+ scattering rate, given by $g = 1.53 \times 10^{-15}$ F s^{-1}, estimated from information in *Meier* [1991]. This method of conversion from EUV image photon count to He^+ column-integrated density was originally documented by *Gallagher et al.* [2005] and a more detailed explanation of its origin can be found in that work.

[26] The solar flux data must be taken into account, as EUV images taken at different times of the year could potentially have different brightness values primarily due to differences in solar flux, since the instrument detects resonantly scattered EUV originating from the sun. For this study, we used 10-min averaged solar flux measurements made by the Solar Extreme Ultraviolet Monitor (SEM) instrument onboard the Solar Heliospheric Observatory (SOHO) spacecraft. These data are spectrally centered at 30.4 nm, though the flux measured actually ranges from 26 nm to 34 nm [*Judge et al.*, 1998, 2002].

[27] Figure 5 shows the flux tube journeys for event 2001/173/01:24–10:37. Each connected set of points represents the column abundance of a single flux tube tracked as it rotates around the Earth. In this event, we applied the 0.85 corotation factor determined by our automated technique. Each data point on a given tube is in a different EUV

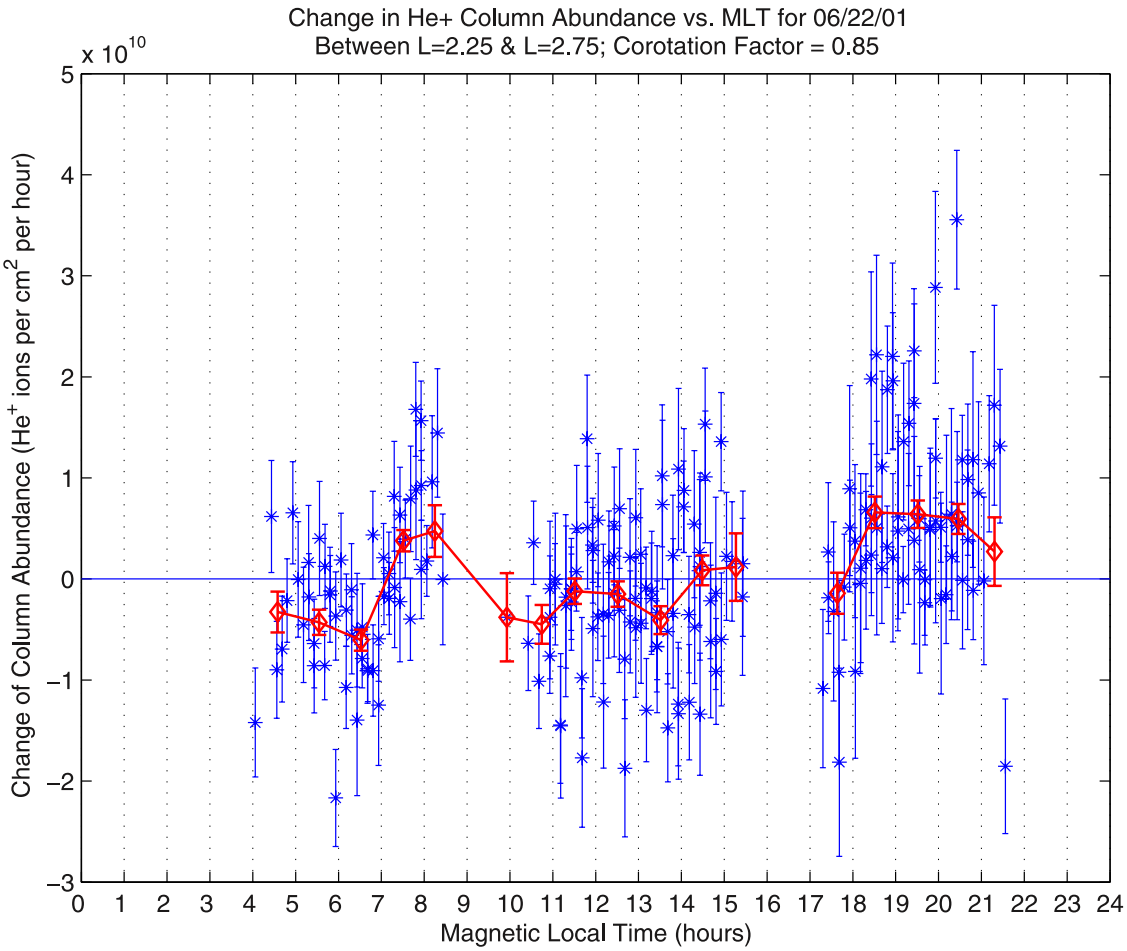

Figure 6. Change in He^+ column abundance along the EUV line of sight as a function of local time. The error bars on the individual values are derived from the column abundance uncertainties seen in Figure 5. The red diamond curve represents the weighted mean of the change in column abundance values, binned hourly, with the standard deviation of the mean as error bars.

image, one after another. The gaps around mid morning and mid afternoon are due to the EUV image seam effects, and the gap from MLT 22 to MLT 02 is due to the Earth's shadow. The error bars are the standard deviation of the mean He^+ column abundance, derived from the pixels contained in one of the 128 azimuthal bins. Thus the uncertainty in our measurement of the mean column abundance is $\sigma/(n)^{1/2}$, where σ is the standard deviation of the column abundance values of the pixels in a binned region of an original, unmapped EUV image, and n is the number of independent pixel column abundance values in that bin. It is worth mentioning that the version of the EUV image that is mapped to the geomagnetic equator will have a higher number of pixels in an azimuthal bin, since the mapping process stretches the image by duplicating pixels from the original unmapped EUV image. Hence to obtain the number of independent measurements, n, we take the total number of pixels inside the azimuthal bin on the mapped image, and count the number of different brightness values among those pixels.

[28] The event shown in Figure 5 depicts a rise in density shortly after dawn (MLT = 6), a stagnation in the hours surrounding local noon, and another rise in density in the mid-afternoon through dusk and into the evening. We will show that, though the flux tube He^+ column abundance varied from one event to another, the median behavior of He^+ column abundance in our 128 events follows the same trend. It is also interesting to note that there is a net increase of ~100% from the average column abundance levels in the early morning, say MLT ~ 5, to the levels in the late evening. This implies that column abundance drops significantly as the flux tube rotates around the night side of the Earth, perhaps via dumping of plasmaspheric He^+ into the ionosphere, because of the lower night time plasma pressure in the ionosphere.

[29] Since we are unable to observe a flux tube uninterrupted for more than about 10 h, due to the constraints of IMAGE's orbit, and since each flux tube will have its own unique starting and ending column abundance along an EUV line of sight, we must be cautious when using figures like Figure 5 to interpret the behavior of a flux tube over more than 10 h of local time. A more useful result would be the rate of increase or decrease in density on a flux tube as a function of local time. We can obtain this by taking the

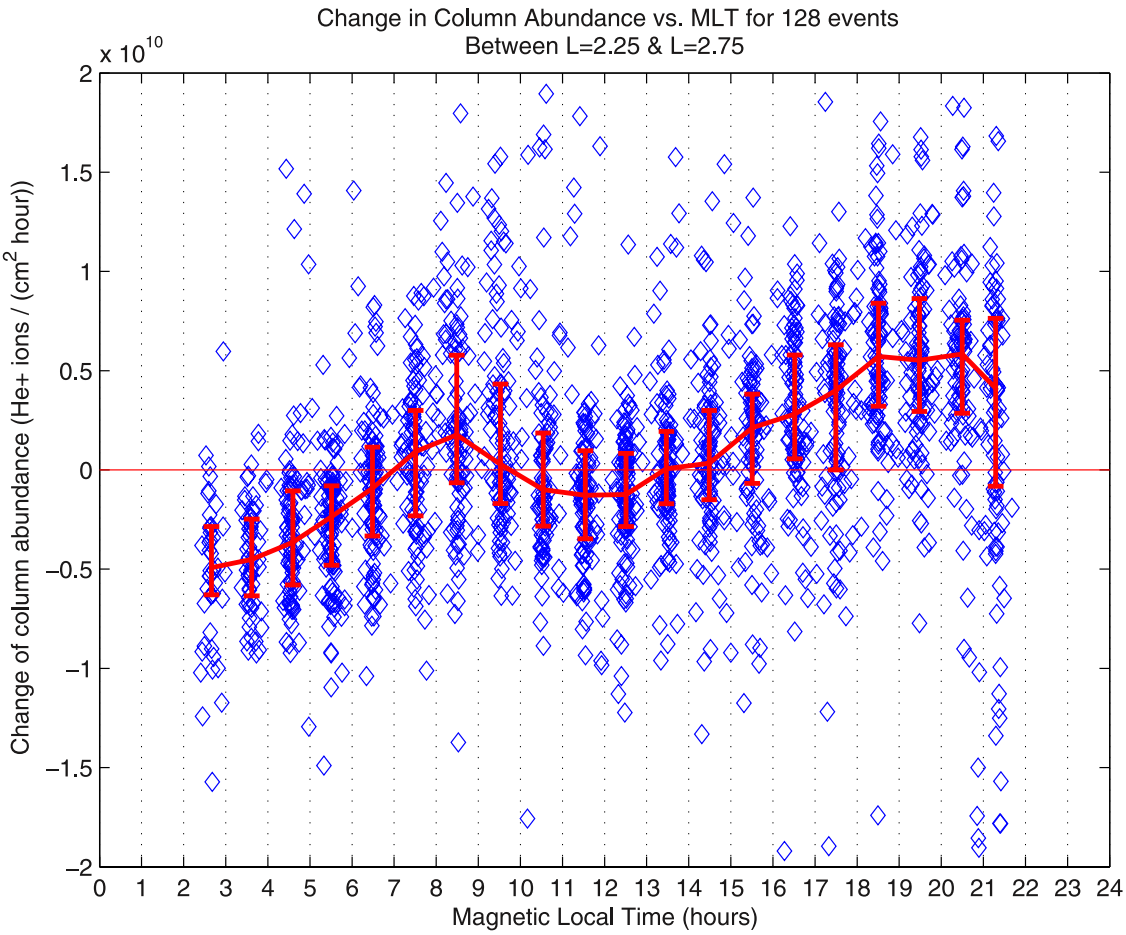

Figure 7. Change in the column abundance of He^+ ions as a function of MLT for the 128 IMAGE passes selected out of the 2001 EUV database. The solid red curve represents the median trend in filling rates: positive (into the flux tube) above the zero line, and negative (out of the flux tube) below it. Error bars indicate quartile values.

slope of the flux tube journey column abundance profiles to produce profiles of the change in EUV line-of-sight column abundance vs. local time for each flux tube, in units of He^+ ions per cm^2 per hour. Figure 6 shows the change of line-of-sight column abundance obtained by taking the time derivative of the flux tube journeys in Figure 5. The error bars on each of the change in column abundance values are derived from the column abundance uncertainties seen in Figure 5, and are ultimately due to the standard deviation of the mean pixel brightness in each of the 128 azimuthal bins. The slopes of the many flux tubes at a given MLT are averaged together in hourly bins, producing the red diamond curve, which represents the weighted mean of the change in line-of-sight column abundance as a function of local time. A positive change in column abundance (from one value to the next) is interpreted as an increase in He^+ density in the flux tube, while a negative change in brightness is assumed to mean a decrease in He^+ density in that flux tube. Hence Figure 6 can be thought of as a proxy for upward flow of He^+ into the plasmasphere (positive values) and downward flow of He^+ out of the plasmasphere, presumably into the ionosphere (negative values).

2.6. Single Image Profiles

[30] In addition to our method of following flux tubes using measured plasmaspheric rotation rates, we have studied the average behavior of the He^+ distribution in local time in single EUV images. That is, we look at the local-time-dependent brightness profile of each of our EUV images individually, and then combine those results to look at the azimuthal variation of He^+ column abundance on average. This differs from our approach of following the flux tubes in that we are merely looking at azimuthal column abundance profiles from single images, not a succession of images. It cannot tell us what is happening in a particular flux tube over diurnal time scales, but it can give an indication of where in MLT the He^+ column abundances are the highest and lowest.

3. Results

3.1. Diurnal Variation

[31] The aforementioned procedure was carried out for all 128 events listed in Appendix A, and the mean change in column abundance for each event was combined with the mean change of all other events. Excepting a few outliers,

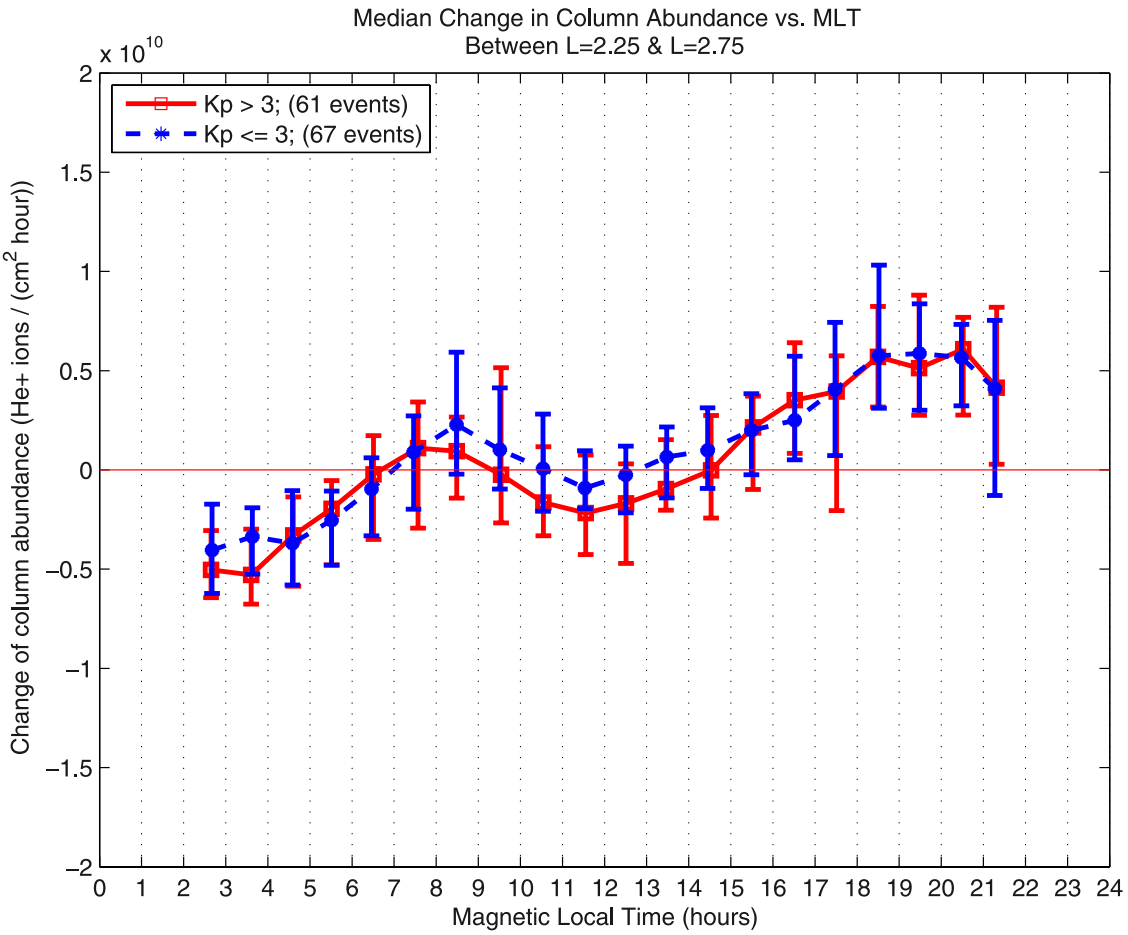

Figure 8. Median values with quartile error bars for the change in line-of-sight column abundance of He^+ for events during high (solid red curve) and low (dashed blue curve) geomagnetic activity.

these means of each event, placed at the mean change in brightness value and mean local time for each hourly MLT bin (i.e., one mean value for all change-in-brightness values between MLT 9 and 10, between 10 and 11, etc.) are plotted together in Figure 7. Each diamond point represents the mean change in column abundance, in units of He^+ ions cm^{-2} h^{-1}, at that MLT for one of the 128 events. The solid curve passes through the median values of the mean change in column abundance, binned hourly, for all 128 events. Error bars represent quartile values for each bin.

[32] Figure 7 shows that, though behavior on any particular day is hard to predict because of large variability, an overall diurnal trend does emerge:

[33] 1. During the pre-dawn morning sector, He^+ density is mostly decreasing (values are below zero).

[34] 2. During the post-dawn to mid-morning sector, brightness tends to be increasing. This seems intuitive given that the flux tube's ionospheric end has entered sunlight at that time, and solar photoionization and energization likely increases the outward pressure, causing He^+ ions to move outward filling the flux tube.

[35] 3. There is a stagnation around noon, where the scattered values are centered around zero change in column-integrated density.

[36] 4. EUV brightness tends to be increasing from mid-afternoon, through dusk, and into the evening.

[37] Our 128 events were chosen primarily for the quality of the EUV image data, and so they cover a range of geomagnetic activity levels. In Figure 8, we show the effect of geomagnetic activity on the increase or decrease in He^+ column abundance of the plasmasphere. We have separated the scattered data points from Figure 7 into those events where Kp never rose above 3 during the time range of the event's images or in the 24 h preceding the earliest image, and those events where Kp did rise above a value of 3 at some point during that time period. Of the 128 total EUV events, 67 events had Kp $\leq$ 3, 61 events had Kp > 3. As can be seen in Figure 8, the median curves from each of these geomagnetic activity levels are within each other's quartile error bars, indicating that the diurnal rate of change of density in a plasmaspheric flux tube does not seem to depend heavily on geomagnetic activity. Hence geomagnetic activity does not appear to have a significant effect on diurnal refilling rates.

[38] To explore the L-shell dependence of the diurnal variation, we further review our 128 events for cases where the quality of the EUV images is high enough in the outer regions to allow an observation of the variation at L = 3.5. The outer regions of the plasmasphere can be distorted in

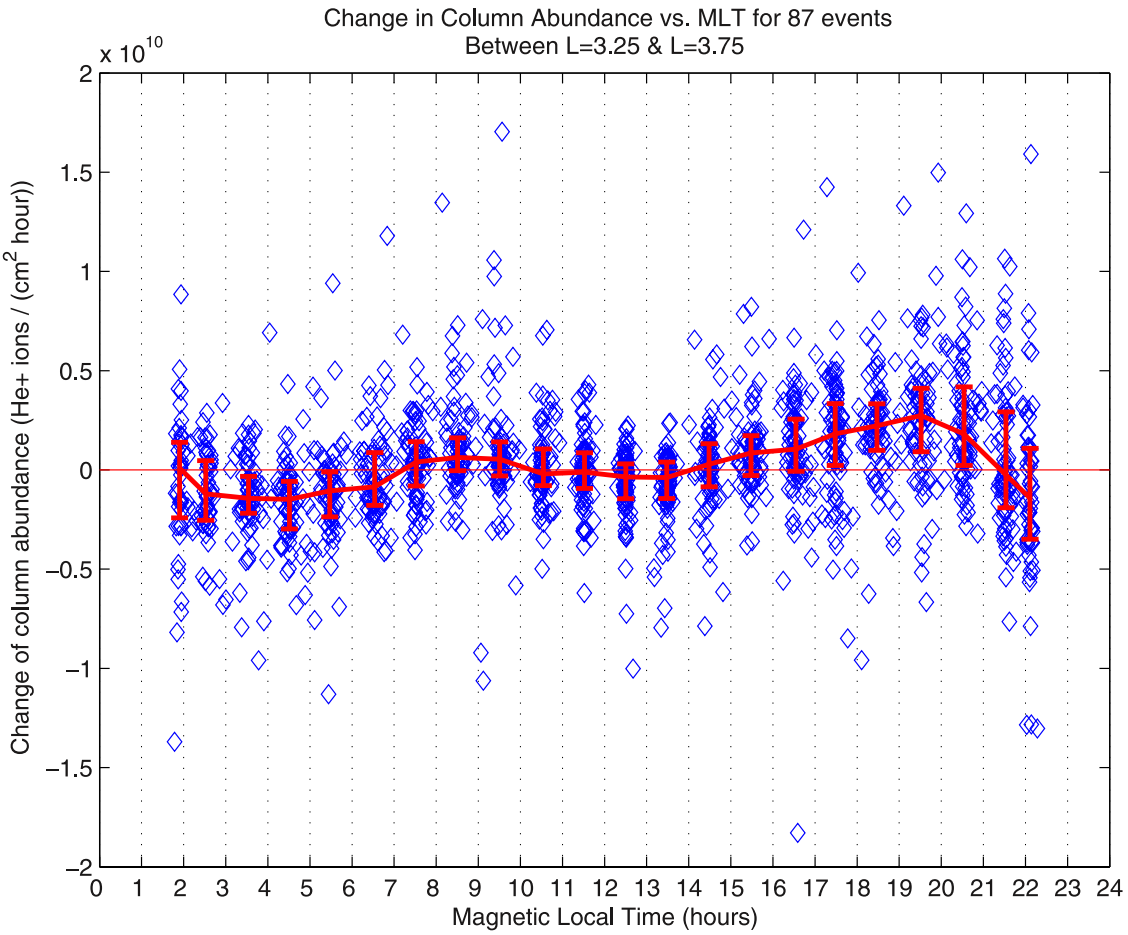

Figure 9. Change in column abundance of He^+ for 87 events that were suitable for diurnal variation analysis at an average L-shell of 3.5. The central curve represents the median, binned hourly, with quartile error bars.

mapped EUV images, especially at the low-latitude limits of the IMAGE pass, because of the geometry of EUV's field of view. As a criteria for using the event at L = 3.5, we take profiles from all 128 events in an annulus ranging from L = 3.25 and L = 3.75, and eliminate events where no cross-correlations yield coefficients above 0.5. This leaves us with 87 events suitable for diurnal variation study at L = 3.5. Figure 9 shows the results of this study, analogous to Figure 7. Again, we have scaled this figure between $\pm 2 \times 10^{10}$ He^+ ions cm^{-2} s^{-1}. Note that there is still a detectable diurnal variation at L = 3.5, however it is much less dramatic than that that observed at L = 2.5.

3.2. Single Image Profiles

[39] Figure 10 shows the mean and median azimuthal column abundance profiles for all 1079 individual EUV images used in our study. Each EUV image profile was extracted as an average brightness at L = 2.5, and the photon counts were converted to He^+ column abundances. The values in each profile have been normalized to the value at MLT = 6 (dawn) for that profile, such that the Y-axis gives a ratio of the column abundance at a given MLT to the value at dawn for that same image. Though the scatter in the individual image profiles is large, it is clear that, on average, the dusk and evening sectors are significantly brighter than the dawn region. The mean and median column abundance appears to peak around MLT = 20, slightly after dusk, and the peak column abundance tends to be about 50%–100% higher than the value at dawn.

[40] Figure 11 shows the mean and median curves azimuthal column abundance profiles for the 734 individual EUV images that were deemed usable for observing diurnal variation at L = 3.5. At this outer L-shell, the annulus may partially sample the plasma trough or the plasmapause instead of the interior of the plasmasphere. Also, since L = 3.5 is closer to the edge of the EUV field of view than is L = 2.5, the annulus may sometimes sample blacked out regions of the EUV image in one MLT region, while sampling typical plasmaspheric brightness values in another. Hence there are many profiles in this data set with unreasonably high or low values, due mainly to poor sampling conditions in that part of the EUV image. The mean curve is too heavily influenced by off scale high and low individual profiles, and so is thought to be unrepresentative of the real diurnal variation at L = 3.5. The median profile, however, shows the same familiar trends that can be seen at L = 2.5. The column abundance peaks in the post-dusk region, and

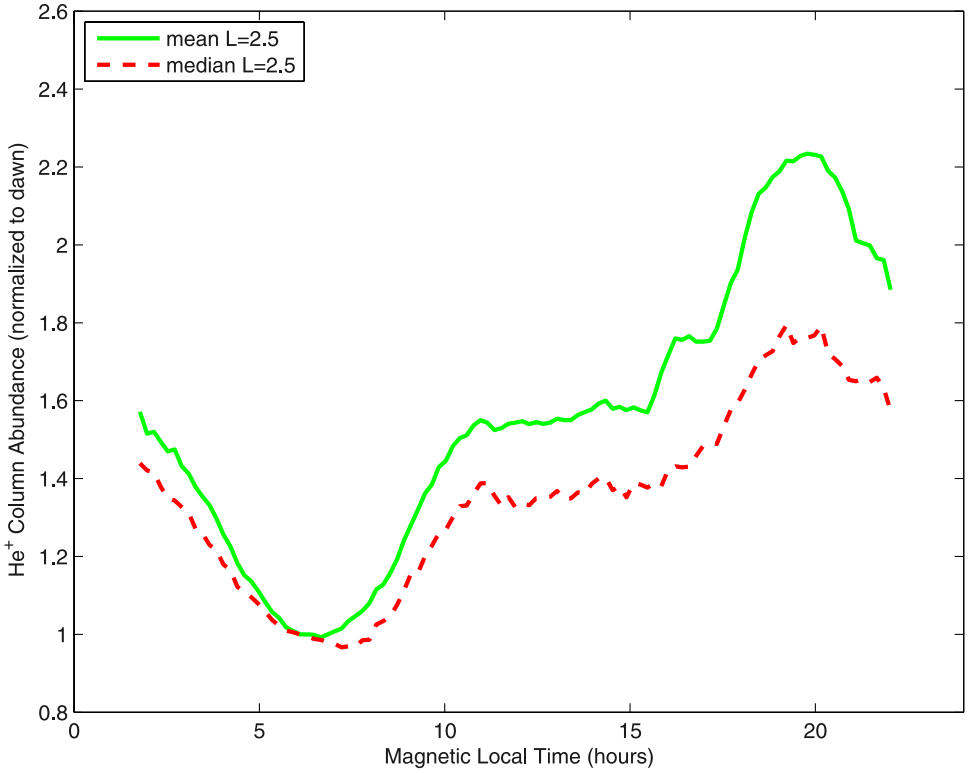

Figure 10. The mean and median of the 1079 single image He^+ column abundance profiles that fall within the time ranges listed in Appendix A, taken at L = 2.5. The solid curve is the mean of all 1079 single image profiles, binned into 128 MLT divisions, and the dashed curve is the median.

the peak values are over 100% higher than the column abundance at dawn.

4. Discussion

[41] There are several main observations to be drawn from our study of diurnal variation of He^+ density using IMAGE EUV brightness changes: (1) a general increase in density from dawn to dusk across the dayside of about a factor of 2, (2) a clear rise in the He^+ column abundance in plasmaspheric flux tubes immediately after dawn, and (3) a stagnation or local minimum in the brightness increase in the few hours surrounding local noon. These observations appear to be consistent when analysis was performed on the images at L = 2.5 and L = 3.5.

[42] *Park et al.* [1978] concluded from whistler observations that the diurnal variation in outward flux of electrons from the ionosphere was not enough to affect the average density along plasmaspheric flux tubes outside of L = 3 on a diurnal time scale. They did detect a diurnal variation at L = 3, but found that diurnal effects are obscured by relatively large day-to-day variations due to storm and substorm effects. We, however, see a small but clear diurnal variation in He^+ column abundance at L = 3.5. As seen by comparison of Figures 7 and 9, the diurnal variation of column abundance at L = 3.5 is less dramatic than at L = 2.5. However, it is important to note that the rates we have shown here are absolute rates of change in column abundance. Though the change in units of He^+ cm^{-2} s^{-1} is significantly smaller at L = 3.5, the ratio of the refilling rate to the column abundance itself appears to be similar at the two different L-shells.

[43] To see this, we can ask how we would expect the refilling rate to vary with L-shell. We might expect that the supply rate of outflowing ions from the ionosphere (per unit area) is roughly constant with latitude. Given that assumption, we would expect the equatorial volume refilling rate to be inversely proportional to the volume of a magnetic flux tube. Since a dipolar magnetic flux tube has a volume that depends on L^4, we would expect the volume refilling rates in our study to differ by a factor of $(3.5/2.5)^{-4} = 0.26$; i.e.: the volume refilling rate at L = 3.5 should be 26% of the volume refilling rate at L = 2.5. Our observations in this study are not volume refilling rates, however, but column abundance refilling rates. We can obtain the ratio of changes in column abundance at L = 3.5 to those at L = 2.5 by multiplying the ratio of volume refilling rates (0.26) by the ratio of the length of the EUV line of sight passing through L = 3.5 to the line of sight passing through L = 2.5. Assuming a typical polar viewing geometry of the IMAGE spacecraft, we find that we would expect the column abundance refilling rate at L = 3.5 to be ~0.36 of that at L = 2.5, simply because of the different volumes of the outer and inner flux tubes. When we compare the median column abundance refilling rates shown in Figures 7 and 9, we find that the curves align quite well with one another when the L = 3.5 data is scaled up by a factor of 2.5 (see Figure 12). Thus we observe that the column abundance refilling rate at

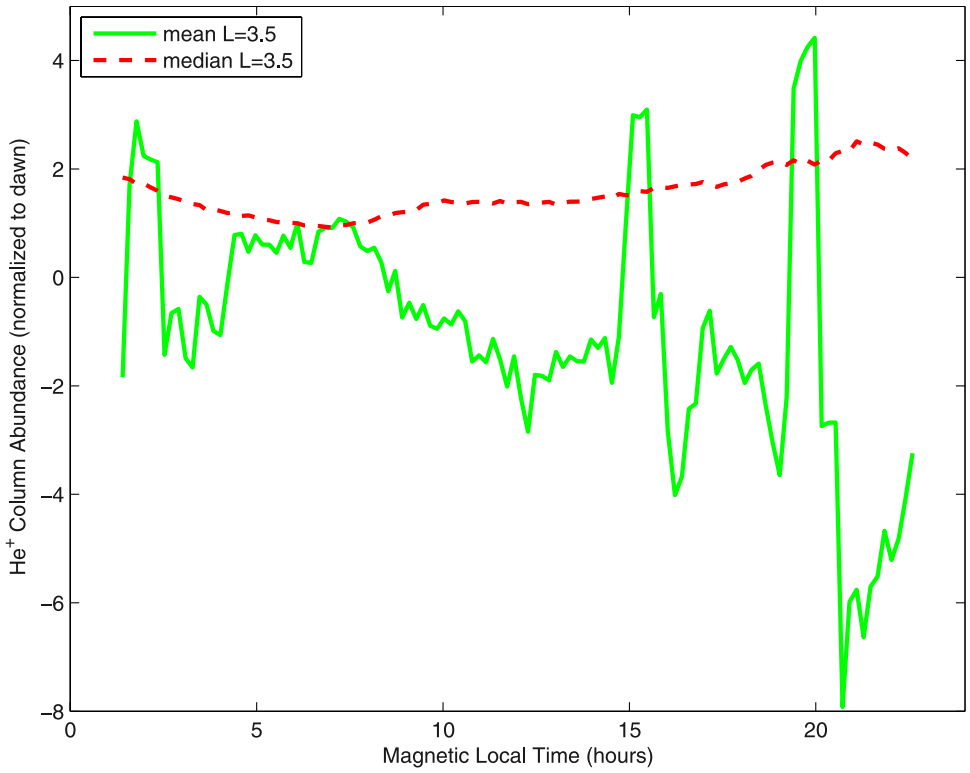

Figure 11. The mean and median of the 734 single image He^+ column abundance profiles deemed viable for analysis at L = 3.5, binned into 128 MLT divisions.

L = 3.5 is about (1/2.5 =) 0.4 times the rate at L = 2.5. This is close to the ratio we would expect because of the difference in flux tube volume alone (0.36). Hence though diurnal variation at outer plasmaspheric flux tubes may be difficult to observe because of the low absolute refilling rates resulting from high flux tube volume, the ratio of the refilling rate to the column abundance appears to be similar to lower L values. Diurnal variation can, in fact, be observed at L-shells beyond L = 3.

[44] The general increase in density across the dayside is consistent with ground-based magnetometer observations of plasma mass density made by [*Moldwin and Berube*, 2004]. *Menk et al.* [1999] conducted a study using ULF field line resonance techniques to measure plasma mass density over several days, and compared with electron density derived from VLF whistler measurements. They found that, during periods with little variation in geomagnetic activity, the electron and mass densities tended to increase somewhat uniformly from dawn to dusk, and then began decreasing soon after 18 MLT. These observations were consistent with a modeling study of ULF pulsation eigenperiods by *Poulter et al.* [1988]. Interestingly, Poulter et al. showed that, when E × B drift measurements are included in the model predictions, the eigenperiods (which are proportional to mass density) usually peak near 18 LT in the inner plasmasphere, but can result in a mid-day minimum at latitudes higher than ∼35° (L>4), because of azimuthal electric fields convecting flux tubes to different latitudes. Menk et al. did not see this effect at L-shells lower than 4, consistent with Poulter et al., however we do observe a noontime stagnation in the change of He^+ density at L = 2.5 and L = 3.5. An advantage of the present work is that it accounts for the important effect of subcorotation, while the ground-based techniques cannot, since the magnetometer array is corotating with the Earth, and so a purely corotational plasma environment must be assumed.

[45] The stagnation in brightness variation at or around local noon in comparison to the distinctly positive change in column abundance just after dawn may be related to a daily minimum in upward plasma flux at local noon in the topside ionosphere. *Richards and Torr* [1985] investigated H^+ upward flux from the ionosphere using a model, originally developed by *Bailey et al.* [1979], which numerically solves the momentum and continuity equations for O^+ and H^+ in the topside ionosphere. Richards and Torr propose that a maximum around 6 LT is due to a rapid increase in O^+ scale height because of heating by photoionization. They also note that a noon minimum in upward H^+ flux at the topside ionosphere is due to a minimum in topside ionospheric H^+ concentration at that time. Neither paper discusses He^+, but they do show that there are interesting variations in the upward flux of both light (H^+) and heavy (O^+) ions on diurnal time scales. If the topside ionosphere, the source region for the plasmasphere, has a minimum concentration of He^+ at local noon, it would follow that there would be a minimum in upward He^+ flux into the plasmasphere at that time, which could be observable as a local minimum or stagnation in the variation of He^+ column abundance along EUV lines of sight passing through flux tubes around noon MLT. Our current study observes such a stagnation, though any statement regarding the cause of this stagnation at the moment remains an untested hypothesis. Further investiga-

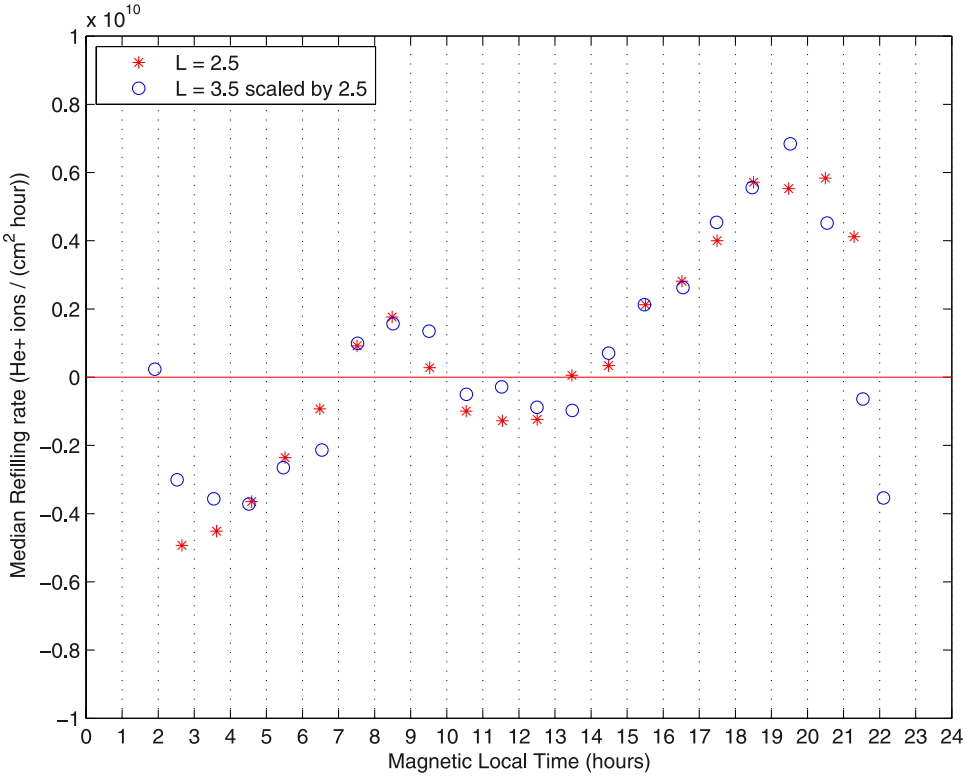

Figure 12. Median change in column abundance from L = 2.5 (asterisks) and L = 3.5 (circles), but with the L = 3.5 values multiplied by a scaling factor of 2.5. Other than the scaling factor, these values are the same as the median values in Figures 7 and 9.

tion into the noon-time concentration of He^+ in the ionosphere is required if the noon-time stagnation observed in our study is to be better understood.

[46] *Saxton and Smith* [1989] used observations of whistlers at conjugate points to VLF transmitters to infer the flux of electrons from the ionosphere to the plasmasphere. On the whole, they found that electron fluxes were directed upward starting shortly after one end of a flux tube enters sunlight (the other end may still be in darkness, depending on the season). They also found that emptying of the flux tube via net downward electron flux begins as soon as one of the ends of a given flux tube enters darkness. The implication is that, with net downward fluxes beginning at dusk, plasmaspheric densities should start declining at that time as well. We do not observe such a decrease in the EUV data. Instead, the continued increase in EUV brightness through dusk into evening suggests that He^+ density continues to rise well into the evening. The fact that our data is centered around the summer season, during which there is a North-South asymmetry in received sunlight at a given magnetic latitude, may mean that one of the flux tube's ionospheric ends could still be in sunlight while the other is not, allowing the outward flow to continue even after the flux tube has passed 18 MLT. It is interesting, however, that the opposite effect does not appear to be taking place on the dawn side, where the change in column abundance goes from negative to positive fairly consistently at 6 MLT.

[47] Another possibility is that the dusk-side "bulge" of the plasmasphere is playing a role in these EUV image observations, such that our circular annulus overlaid on the image is straying into lower L-shells, and thus higher He^+ densities in the region from late afternoon through the evening. If this is the case, it would be interesting in and of itself, since E × B drift paths at such low L-shells as 2.5 should be nearly circular during moderate and quiet periods of geomagnetic activity. Of the 128 events used in this study, about half had $Kp \geq 3$, and half had $Kp < 3$. The change in He^+ column abundance for both these high Kp events and the low Kp events is shown in Figure 8. The general trend observed for all the events is still visible for both the high activity and low activity events, with no discernible difference between the two activity levels.

[48] The issue of what happens to the He^+ density that has been accumulated since dawn when the plasmaspheric flux tube moves across the night region will be further addressed in a future study, but it is clear that the flux tube content must eventually decrease, since there is such a clear difference between the early morning and late evening line-of-sight column abundance values in Figures 5 and 10. Also, though we omit data from the portion of the EUV images in the Earth's shadow, we consistently observe negative changes in column abundance in the pre-dawn sector, as shown in Figures 7, 8, and 9, which implies negative filling rates for plasmaspheric flux tubes in much of the night region, where ionospheric plasma pressure is lower because of lack of solar photoionization. Also, by averaging the change in column abundance values for all our events (the diamonds in Figures 7 and 9), we can obtain an estimate of the plasmaspheric He^+ refilling rate averaged over MLT (excluding the region of the EUV images in the

Earth's shadow, between about 22 and 02 MLT). We find that the refilling rate averaged over all available MLT is $0.088 \times 10^{10} \pm 0.016 \times 10^{10}$ He^+ ions cm^{-2} h^{-1} at L = 2.5, and $0.027 \times 10^{10} \pm 0.008 \times 10^{10}$ He^+ ions cm^{-2} h^{-1} at L = 3.5. The uncertainties given here are the standard deviations of the means. These refilling rates averaged over MLT are quite small when compared to the median peak refilling rates of $\sim 0.5 \times 10^{10}$ He^+ ions cm^{-2} h^{-1} for L = 2.5 and $\sim 0.25 \times 10^{10}$ He^+ ions cm^{-2} h^{-1} for L = 3.5, which are larger than the MLT-averaged refilling rates by a factor of $\sim$8 and 10, respectively. Given that $\sim$4 h of MLT are not sampled, and that those late night hours would be expected to yield negative filling rates, it is likely that the net refilling rate averaged over 24 h of MLT is close to zero, which would again imply that plasmaspheric He^+ is being lost to the ionosphere as the flux tubes move across the night side of the Earth.

[49] Finally, the mean and median of many single image profiles, displayed in Figures 10 and 11, represent a different method of globally observing diurnal variation using the same set of images. Yet, even in individual EUV images, the general trend we have observed in the flux tube tracking method is evident: decreasing column abundance in the pre-dawn sector, sharply increasing post-dawn, a stagnation or even decrease around local noon, and a sharp increase into the afternoon and past dusk. Both the mean and median curves at L = 2.5 (Figure 10), as well as the median curve at L = 3.5 (Figure 11) show a flattening of the azimuthal change in column abundance around noon, which corresponds to the small or even negative refilling rates observed using the flux tube tracking method.

5. Conclusions

[50] In general, the column abundance flux tube journeys, change in column abundance as a function of MLT, and individual EUV image profiles presented here indicate a rise in He^+ density in the morning sector, a stagnation around noon, and then a rise in the afternoon sector through dusk and into the evening. The general trend of rising plasmaspheric density from dawn to dusk is attributed to plasmaspheric filling by photoionization at the ionospheric ends of flux tubes. The noon stagnation agrees with field line resonance observations by *Moldwin and Berube* [2004], and is thought to be related to a noontime minimum in the concentration of neutral species in the ionosphere [*Richards and Torr*, 1985]. Profiles from 1079 individual EUV images centered around northern summer of 2001 showed that mean column abundance for this data set peaks around MLT = 20, slightly after dusk, and the peak column abundance tends to be about 1.5–2 times the value at dawn.

[51] We have shown that a variation in plasmaspheric He^+ density is observable over diurnal time scales in EUV data at L = 2.5 and to a lesser extent at L = 3.5. This study provides the first global observations of the diurnal refilling trend of plasmaspheric flux tubes by photoionization at the ionosphere.

Appendix A

[52] Table A1.

Table A1. The 128 Passes of the IMAGE Spacecraft in the Year 2001 During Which Useful EUV Data Were Found to Exist for Durations Greater Than or Equal to 6 h

Day	UT	Day	UT	Day	UT
120	0828–1537	161–162	1929–0239	189–190	1658–0008
120–121	2235–0443	162	0947–1758	190	0727–1437
121	1201–1911	162–163	2304–0817	190–191	2034–0547
124	1138–1848	163	1353–2204	191	1144–1854
125	0156–0814	164	0330–1243	192	0009–1024
127	1106–1815	165	0918–1628	192	1529–2239
128	0123–0731	165–166	2225–0738	193	0649–1359
128	1530–2139	167	0251–1204	193–194	1956–0407
138	0312–0920	167–168	1710–0121	194	1106–1826
138	1720–2328	168	0728–1641	195	1512–2222
139	0717–1427	168–169	2146–0659	196	0622–1332
139–140	2135–0445	169	1246–1955	196–197	1939–0350
140	1051–1902	170	0223–1034	197	0957–1707
141	0211–0920	171	0832–1542	197–198	2324–0837
141	1608–2216	171–172	2037–0550	198	1403–2124
142–143	2004–0313	172	1147–1856	199	0513–1223
143	1031–1741	173	0124–1037	199–200	1820–0140
144	0049–0900	173–174	1553–0004	200–201	2307–0718
144	1447–2207	174	0611–1422	201	1447–2106
145	0444–1255	174–175	2120–0430	202–203	1813–0123
145–146	2024–0232	175	1037–1849	204	0011–0620
146	0930–1640	176	0106–0917	204	1258–2008
146–147	2359–0708	176	1535–2143	205	0144–0955
148	0435–1256	177	0644–1354	205–206	1654–0004
148–149	1812–0121	177–178	1850–0301	206	0712–1523
149	0931–1641	179	0007–0829	206–207	2019–0532
149–150	2238–0649	179	1446–2206	207	1209–1919
150	1347–2057	180	0454–1306	208	0248–0958
151	0324–1135	180–181	1811–0223	208	1555–2305
151–152	1752–0102	181	0931–1641	209	0725–1334
152	0810–1622	181–182	2248–0700	209–210	2042–0352
152–153	2218–0528	182	1439–2058	210	1142–1800
153	1236–1946	183	0346–1157	212	0505–1316
154	0214–1025	183–184	1754–0104	212–213	2014–0324
154–155	1652–0012	184	0924–1634	213	1012–1722
155	0710–1521	184–185	2231–0642	213–214	2340–0801
155–156	2118–0428	185	1320–2030	214	1621–2230
156	1136–1948	186	0308–1119	215–216	1835–0145
157	0103–0915	186–187	1716–0026	216–217	2210–0621
157	1542–2252	187	0836–1546	217	1340–2050
158	0600–1411	187–188	2051–0604	218–219	1705–0127
158–159	2008–0318	188	1252–2012	219	0835–1545
161	0511–1322	189	0139–1051		

[53] **Acknowledgments.** This research was supported by a NASA Graduate Student Research Program (GSRP) fellowship (grant NNG05GL87H) and a NASA Guest Investigator grant (NNG04GG43G). The authors thank Terry Forrester for his insightful comments and discussion regarding the EUV data itself as well as IDL EUV analysis tools available at http://euv.lpl.arizona.edu/euv/index.html. The authors thank USC Space Sciences Center for providing SEM data. SOHO is a project of the international cooperation between ESA and NASA (http://www.usc.edu/dept/space_science/instrument_pages/sem.htm). Work at the University of Arizona was funded by a subcontract from Southwest Research Institute under NASA contract NAS5-96020 with SwRI, and by NASA grant NNX07 AG46G. The authors acknowledge important improvements to the manuscript resulting from the insightful comments of the reviewers.

[54] Zuyin Pu thanks Dennis Gallagher and another reviewer for their assistance in evaluating this paper.

References

Bailey, G. J., R. J. Moffett, and J. A. Murphy (1979), Calculated daily variations of O^+ and H^+ at mid-latitudes. II: Sunspot maximum results, *J. Atmos. Terr. Phys.*, *41*, 417–429.

Berube, D., M. B. Moldwin, and M. Ahn (2006), Computing magnetospheric mass density from field line resonances in a realistic magnetic field geometry, *J. Geophys. Res.*, *111*, A08206, doi:10.1029/2005JA011450.

Burch, J. L., J. Goldstein, and B. R. Sandel (2004), Cause of plasmasphere corotation lag, *Geophys. Res. Lett.*, *31*, L05802, doi:10.1029/2003GL019164.

Carpenter, D. L., and R. R. Anderson (1992), An ISEE/whistler model of equatorial electron density in the magnetosphere, *J. Geophys. Res.*, *97*(A2), 1097–1108.

Clilverd, M. A., et al. (2003), In situ and ground-based intercalibration measurements of plasma density at L = 2.5, *J. Geophys. Res.*, *108*(A10), 1365, doi:10.1029/2003JA009866.

Foster, J. C., P. J. Erickson, A. J. Coster, J. Goldstein, and F. J. Rich (2002), Ionospheric signatures of plasmaspheric tails, *Geophys. Res. Lett.*, *29*(13), 1623, 10.1029/2002GL015067.

Gallagher, D. L., M. L. Adrian, and M. W. Liemohn (2005), Origin and evolution of deep plasmaspheric notches, *J. Geophys. Res.*, *110*, A09201, doi:10.1029/2004JA010906.

Garcia, L. N., S. F. Fung, J. L. Green, S. A. Boardsen, B. R. Sandel, and B. W. Reinisch (2003), Observations of the latitudinal structure of plasmaspheric convection plumes by IMAGE-RPI and EUV, *J. Geophys. Res.*, *108*(A8), 1321, doi:10.1029/2002JA009496.

Goldstein, J., M. Spasojevic, P. H. Reiff, B. R. Sandel, W. T. Forrester, D. L. Gallagher, and B. W. Reinisch (2003), Identifying the plasmapause in IMAGE EUV data using IMAGE RPI in situ steep density gradients, *J. Geophys. Res.*, *108*(A4), 1147, doi:10.1029/2002JA009475.

Goldstein, J., B. R. Sandel, M. F. Thomsen, M. Spasojevic, and P. H. Reiff (2004), Simultaneous remote sensing and in situ observations of plasmaspheric drainage plumes, *J. Geophys. Res.*, *109*, A03202, doi:10.1029/2003JA010281.

Grew, R. S., F. W. Menk, M. A. Clilverd, and B. R. Sandel (2007), Mass and electron densities in the inner magnetosphere during a prolonged disturbed interval, *Geophys. Res. Lett.*, *34*, L02108, doi:10.1029/2006GL028254.

Guiter, S., T. Gombosi, and C. Rasmussen (1991), Diurnal variations on a plasmaspheric flux tube: Light ion flows and F region temperature enhancements, *Geophys. Res. Lett.*, *18*(5), 813–816.

Judge, D. L., et al. (1998), First solar EUV irradiances obtained from SOHO by the CELIAS/SEM, *Sol. Phys.*, *177*, 161–173.

Judge, D. L., H. S. Ogawa, D. R. McMullin, P. Gangopadhyay, and J. M. Pap (2002), The SOHO CELIAS/SEM EUV database from SC23 minimum to the present, *Adv. Space Res.*, *29*(12), 1963–1968.

Meier, R. R. (1991), Ultraviolet spectroscopy and remote sensing of the upper atmosphere, *Space Sci. Rev.*, *58*, 1–185.

Menk, F. W., D. Orr, M. A. Clilverd, A. J. Smith, C. L. Waters, D. K. Milling, and B. J. Fraser (1999), Monitoring spatial and temporal variations in the dayside plasmasphere using geomagnetic field line resonances, *J. Geophys. Res.*, *104*(A9), 19,955–19,969.

Moldwin, M. B., and D. Berube (2004), ULF resonance monitoring of diurnal plasmaspheric refilling: Results from the MEASURE magnetometer array, *Eos Trans. AGU*, Spring Meeting 2004, Abstract SM31A-09.

Moldwin, M. B., L. Downward, H. K. Rassoul, R. Amin, and R. R. Anderson (2002), A new model of the location of the plasmapause: CRRES results, *J. Geophys. Res.*, *107*(A11), 1339, doi:10.1029/2001JA009211.

Moldwin, M. B., B. R. Sandel, M. F. Thompsen, and R. C. Elphic (2003), Quantifying global plasmaspheric images with in situ observations, *Space Sci. Rev.*, *109*, 47–61.

Park, C. G., D. L. Carpenter, and D. B. Wiggin (1978), Electron density in the plasmasphere: Whistler data on solar cycle, annual, and diurnal variations, *J. Geophys. Res.*, *83*(A7), 3137–3144.

Poulter, E. M., W. Allan, and G. J. Bailey (1988), ULF pulsation eigenperiods within the plasmasphere, *Planet. Space Sci.*, *36*(2), 185–196.

Richards, P. G., and D. G. Torr (1985), Seasonal, diurnal, and solar cyclical variations of the limiting H^+ flux in the earth's topside ionosphere, *J. Geophys. Res.*, *90*(A6), 5261–5268.

Rishbeth, H. (1972), Superrotation of the upper atmosphere, *Rev. Geophys.*, *10*(3), 799–819.

Roelof, E. C., and A. J. Skinner (2000), Extraction of ion distributions from magnetospheric ENA and EUV images, *Space Sci. Rev.*, *91*, 437.

Sandel, B. R., and M. H. Denton (2007), Global view of refilling of the plasmasphere, *Geophys. Res. Lett.*, *34*, L17102, doi:10.1029/2007GL030669.

Sandel, B. R., et al. (2000), The extreme ultraviolet imager investigation for the IMAGE mission, *Space Sci. Rev.*, *91*, 197–242.

Sandel, B. R., R. A. King, W. T. Forrester, D. L. Gallagher, A. L. Broadfoot, and C. C. Curtis (2001), Initial results from the IMAGE extreme ultraviolet imager, *Geophys. Res. Lett.*, *28*(8), 1439–1442.

Sandel, B. R., J. Goldstein, D. L. Gallagher, and M. Spasojevic (2003), Extreme ultraviolet imager observations of the structure and dynamics of the plasmasphere, *Space Sci. Rev.*, *109*, 25–46.

Saxton, J. M., and A. J. Smith (1989), Quiet time plasmaspheric electric fields and plasmasphere-ionosphere coupling fluxes at L = 2.5, *Planet. Space Sci.*, *37*(3), 283–293.

Yizengaw, E., H. Wei, M. B. Moldwin, D. Galvan, L. Mandrake, A. Mannucci, and X. Pi (2005), The correlation between mid-latitude trough and the plasmapause, *Geophys. Res. Lett.*, *32*, L10102, doi:10.1029/2005GL022954.

D. A. Galvan and M. B. Moldwin, Institute of Geophysics and Planetary Physics, Department of Earth and Space Sciences, University of California 405 Hilgard Ave, Box 951567, Los Angeles, CA 90095, USA. (dgalvan@ucla.edu)

B. R. Sandel, Lunar and Planetary Laboratory, University of Arizona, Sonett Space Sciences Building, 1541 East University Boulevard, Tucson, AZ 85721-0063, USA.